Single-Shot Computational THz 3D Imaging

Abdulraouf Kutaish, Miguel Heredia Conde, Ullrich Pfeiffer

This document is the accepted manuscript version that has been published in final form in:

2024 International Workshop on the Theory of Computational Sensing and its Applications to Radar, Multimodal Sensing and Imaging (CoSeRa)
DOI: https://doi.org/10.1109/CoSeRa60846.2024.10720381

Single-Shot Computational THz 3D Imaging

Abdulraouf Kutaish*, Miguel Heredia Conde† and Ullrich Pfeiffer‡
Institute for High-Frequency and Communication Technology, University of Wuppertal
FE Building, Rainer-Gruenter-Str. 21, 42119 Wuppertal
Email: *kutaish@uni-wuppertal.de, †herediaconde@uni-wuppertal.de, ‡ullrich.pfeiffer@uni-wuppertal.de

***Abstract*—Terahertz (THz) imaging holds promise in a wide range of application fields due to the penetration ability of THz radiation, in combination with a relatively low wavelength, as compared to radar, which facilitates generating sharp images. However, existing THz imaging techniques typically rely on sequential scanning due to the unavailability of large detector arrays. The use of Compressive Sensing (CS) techniques can reduce the number of measurements but does not solve its sequential acquisition. In this work, we show the feasibility of single-shot THz 3D imaging leveraging a multi-aperture THz camera. Adopting a CS perspective, we construct a linear sensing model and assume target sparsity. Our experimental validation confirms that sparsity-promoting methods succeed in reconstructing 3D volumes from a few intensity measurements.**

***Index Terms*—THz imaging, 3D imaging, computational imaging, compressive sensing, sparse reconstruction**

I. Introduction

Non-scanning THz imaging approaches fall into two categories: those using a single detector with computational sensing for image reconstruction, and those using THz detector arrays forming a THz camera. The first category utilizes spatial modulation of THz radiation, leveraging compressive sensing (CS) theory [1]–[3] to efficiently capture information with fewer measurements by exploiting signal sparsity. The second category employs THz lenses and a focal plane array (FPA) of detectors to attain lateral resolution, in the art of optical imaging. However, the larger wavelength of THz radiation and the limitations of THz optics result in broader per-pixel sensing fields, reducing the effective lateral resolution of a THz camera compared to the detector array size.

This issue only gets aggravated when attempting to sense in 3D, as the 3D sensing functions will certainly widen along the range direction. In this work, we aim to close the existing gap between the two mentioned methods of attaining lateral resolution. More specifically, we will rely on a realistic sensing model in order to robustly solve the 3D reconstruction computationally, in the art of computational sensing. Crucially, the necessary measurement diversity is obtained thanks to a multi-aperture configuration leveraging THz FPAs (Focal Plane Arrays), while 3D reconstruction relies on both an accurate sensing model and sparsity of the target, as in CS.

This work received partial funding from the European Research Council (ERC) under the European Union's Horizon 2020 research and innovation programme (grant agreement No 101019972).

II. Related Work

A. Computational Terahertz Imaging

Leveraging CS theory, the single-pixel camera, as demonstrated in [4], allows for reconstructing full-resolution images from a few random projections obtained using a single detector in combination with a Digital Micromirror Device (DMD). Building upon this concept, further research [5] utilizes spatially structured illumination and CS algorithms to eliminate the need for mechanical scanning in THz imaging systems. Through experimental validation, he demonstrates the critical role of precise THz mask projection and the necessity for rigorous calibration to maintain image quality. This concept was extended to obtain CS THz video in [6], using femtosecond-pulsed modulation and demodulation. Additionally, tailored mask design aimed at lowering the coherence of the resulting sensing matrix has been shown to yield superior reconstruction performance in [7], as compared to conventional binary patterns. Multiple regularization techniques for robustly solving the CS THz imaging problem are studied in [8], including Total Variation (TV) and ℓ_1 regularization, also considered in this paper, as well as the use of representation bases or dictionaries to boost target sparsity.

B. 3D and Light Field Terahertz Imaging

An experimental THz imaging setup, incorporating a virtual camera array and a high-power THz source, was developed in [9]. By integrating a novel synthetic aperture approach within the framework of Light Field Imaging, they achieved notable enhancements in image quality and effectively reduced distortion. The process of 3D scene reconstruction in the THz domain, as outlined in [10], involves capturing images from multiple viewpoints to derive depth and spatial relationships. This process includes the identification and matching of features across these images, precise estimation of camera parameters, and the application of triangulation to compute 3D coordinates [10].

Furthermore, dense 3D reconstruction for a 3×3 cube is attempted by means of backpropagation. Although this reconstruction approach is fast, its accuracy is compromised by the non-orthogonality of the sensing model. Light field techniques, traditionally used for visible light, have been applied to THz radiation [11]. This involves the use of camera arrays and masks to capture the comprehensive light field, enabling post-capture image processing techniques such as refocusing and synthetic aperture imaging. This approach significantly

improves the depth of field, dynamic range, and capability to produce true 3D THz images.

III. Methodology

In this section, we introduce our computational THz camera and its sensing model, exploring alternative methods to reconstruct 3D structures from a limited set of incoherent THz measurements.

A. THz Hardware Co-design

Our multi-aperture imaging system comprises independently operating TicWave WS-ID02 THz cameras, courtesy of TicWave-Solutions GmbH. It boasts a frame rate capability of up to 50 frames per second (FPS), a bandwidth of 0.3-1.1 THz, a responsivity of 1G counts/W, and a sensitivity NEP (Noise Equivalent Power) of $10 - 20$ pW$/\sqrt{\text{Hz}}$, both at 320 GHz. A critical advantage of our imaging system lies in its ability to capture 3D information using a multi-aperture FPA, as illustrated in Fig. 1. This configuration enables the system to collect images from multiple perspectives, significantly enhancing depth perception and spatial resolution.

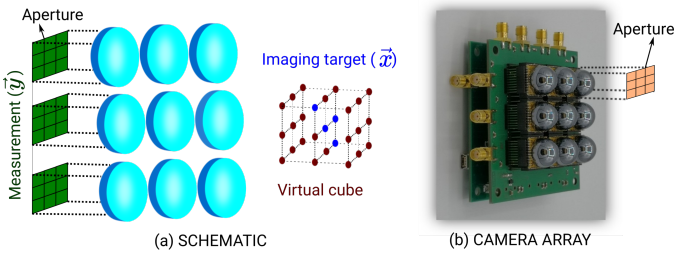

Fig. 1: Schematic representation of the operation of our multi-aperture light-field THz camera.

The THz light-field imaging system shown in Fig. 1 features an array of $P \times Q$ apertures, yielding $N_{\text{a}} = PQ$ identical apertures, each equipped with a silicon lens, and distributed co-planarly on a uniform grid. Specifically, we consider a square multi-aperture system with $P = Q = 3$, resulting in $N_{\text{a}} = 9$. Each aperture contains an FPA of incoherent *THz pixels* of equal size, $n_{\text{rows}} \times n_{\text{cols}}$, yielding $n_{\text{pix}} = n_{\text{rows}} n_{\text{cols}}$ THz pixels per aperture. Therefore, the computational THz imaging sensor can provide up to $m_0 = N_{\text{a}} n_{\text{pix}}$ measurements per exposure. For simplicity, these multi-aperture THz measurements will be regarded as stacked in a single measurement vector $\vec{y_0} \in \mathbb{R}^{m_0}$.

B. Sensing Model

In this work, we focus on a discrete scenario and restrict our attention to a linear sensing model, i. e., each measurement in $\vec{y} \in \mathbb{R}^m$ will be explained as a linear combination of an unknown signal $\vec{x} \in \mathbb{R}^n$, where $n \neq m$ in general. Provided that the ultimate goal is to retrieve the 3D geometry of the observed scene, a uniform discretization of a cubic 3D volume of size $R_x \times R_y \times R_z$ with uniform step $\Delta x = \Delta y = \Delta z$ would yield a 3D tensor $X \in \mathbb{R}^{n_x \times n_y \times n_z}$, where $n_\gamma := R_\gamma / \Delta\gamma$, $\forall \gamma \in \{x, y, z\}$. Then, the unknown vector resulting from restructuring X into vector form is of size $n := \prod_\gamma n_\gamma$. Thus, the hypothesized linear sensing model is given by:

$$\vec{y_0} = \boldsymbol{A_0}\vec{x} + \vec{n}, \tag{1}$$

where $\boldsymbol{A_0} \in \mathbb{R}^{m_0 \times n}$ denotes the sensing matrix that explains $\vec{y_0}$ from $\vec{x}$ and $\vec{n}$ models the measurement noise, which accounts both for a potential model mismatch, detector noise, readout noise, and quantization noise. Without loss of generality, the aggregated noise vector is assumed to follow $\vec{n} \sim \mathcal{N}(0, \sigma)$. Each row of $\boldsymbol{A}$, denoted $\vec{a^i}$, contains a discrete *sensing function*, which linearly explains how each pixel perceives the scene. The model in (1) holds for intensity measurements under incoherent THz illumination. In the case of coherent illumination, $\boldsymbol{A_0}$ models not only the response of the imaging sensor but also the diffracted propagation of light, as explained in [7]. The restriction to incoherent illumination and incoherent detection allows for a phaseless formulation, in which $x_i \in \mathbb{R}^+$, $\forall i$. Furthermore, it also adds to the stability of $\boldsymbol{A_0}$, which can be constructed empirically, leveraging the superposition principle. To this end, the location of a punctual source is swept over the entire signal domain. At each source location, we collect a set of N_{acq} independent measurements. Each measurement follows $\vec{y_0}_k^{(i)} = \boldsymbol{A_0}\vec{x}_k^{(i)} + \vec{n}_k^{(i)}$, for $1 \leq i \leq N_{\text{acq}}$. In this setup, each vector $\vec{x_k}$ is specifically designed to be 1-sparse; it contains a single nonzero element at the k^{th} position (i.e., $\vec{x}_k[i] \neq 0 \iff i = k$), and, for simplicity, this nonzero element is uniformly set to 1. This design ensures that each measurement directly corresponds to the k^{th} source location, which correlates directly to the k^{th} column of $\boldsymbol{A_0}$.

Assuming isotropic emission over an unrestricted field of view (FOV), for N_{acq} large enough, the k^{th} column of $\boldsymbol{A_0}$ can be empirically approximated by:

$$\boldsymbol{A_0} := [\vec{a_0}_k]_{k=1}^n, \quad \vec{a_0}_k \approx \frac{1}{N_{\text{acq}}} \sum_{i=1}^{N_{\text{acq}}} \vec{y_0}_k^{(i)}, \tag{2}$$

with expected ℓ_2 approximation error $\sigma/\sqrt{N_{\text{acq}}} \to 0$ as $N_{\text{acq}} \to \infty$. Details on the experimental procedure followed to empirically obtain the collections of reference measurements $\vec{y_0}_k^{(i)}$ are detailed in section IV-A.

C. Computational 3D Reconstruction

At the light of the sensing model introduced in section III-B, the goal of a computational THz 3D imaging reconstruction method is to obtain an estimate of $\vec{x}$ given a realization of $\vec{y_0}$, exploiting (1) and any available *a priori* knowledge of $\vec{x}$. More specifically, in this paper we demonstrate the impact of considering a *sparsity* assumption on $\vec{x}$, i. e., low $s := |\text{supp}\,(\vec{x})|$, where $\text{supp}\,(\cdot)$ denotes support of a sparse vector. In the following, we outline a set of techniques to solve this inverse problem.

1) Automatic Reduction of the Measurement Space: Lenses are crucial for achieving 2D and 3D resolution, as focusing the light on the FPA yields angular selectivity. Fortunately, the relatively low wavelengths of THz radiation, as compared to

classical radio bands, allow for focusing using silicon lenses. On the other hand, perfect focusing of an image on the FPA would go against the basic principles of CS, which require certain incoherence between the sensing functions and the sparsity basis, which for sparse signals coincides with the trivial basis of $\mathbb{R}^n$. Indeed, it is easy to see that the better the focus, the higher will be the number of uninformative (ideally zero) measurements. Interestingly, quasi-optical THz radiation allows for exploring a turning point, where the existence of a focusing element will project a finite 3D volume ($R_x \times R_y \times R_z$) into a limited region of the FPA, at the time that spatially-varying imperfect focusing spreads the power of sparse targets over wide regions of the measurement space, as required by CS. In this section, we present a preprocessing step that leverages the mentioned fact to further condense the measurement space into $m < m_0$ dimensions. The procedure identifies uninformative sensing functions and eliminates them from the sensing model and is, thus, non-adaptive with respect to $\vec{y_0}$. Given an initial sensing matrix, $\boldsymbol{A_0} \in \mathbb{R}^{m_0 \times n}$, a more compact sensing model is obtained as:

$$\boldsymbol{A} \coloneqq \boldsymbol{A_0}_{(\Omega,:)}, \quad \text{where:} \quad \Omega \coloneqq \left\{ i : \max_j \left(a_{i,j} > \varepsilon\right) \right\}, \quad (3)$$

where ε is a threshold related to model fidelity (thus to $\sigma/\sqrt{N_{\text{acq}}}$). From (1) immediately follows that only the subset of measurements $\vec{y} \coloneqq \vec{y_0}_\Omega \in \mathbb{R}^m$, with $m = |\Omega| < m_0$ will be considered to reconstruct $\vec{x}$.

2) Least-squares Estimation: Even for moderate 3D resolution, the reduced sensing matrix from (3), $\boldsymbol{A} \in \mathbb{R}^{m \times n}$ is wide with $m \ll n$. Consequently, the inverse problem is underdetermined and no unique solution exists. A classical approach is to enforce minimal l_2 norm, i. e., to solve

$$\hat{\vec{x}} = \arg\min_{\vec{x}} \|\vec{x}\|_2 \quad \text{subject to} \quad \vec{y} = \boldsymbol{A}\vec{x}. \quad (4)$$

The solution to (4) is given by the so-called *right* Moore-Penrose pseudoinverse (PI) of $\boldsymbol{A}$:

$$\hat{\vec{x}} = \boldsymbol{A}^\dagger \vec{y}, \quad \boldsymbol{A}^\dagger \coloneqq \boldsymbol{A}^\top \left(\boldsymbol{A}\boldsymbol{A}^\top\right)^{-1} \quad (5)$$

The latter estimator boils down to the back-projection used in [10] ($\hat{\vec{x}} = \boldsymbol{A}^\top \vec{y}$) when $\boldsymbol{A}$ is orthonormal by rows, which is generally not the case.

3) Truncated Singular Value Estimation: Despite the model pruning imposed in (3), measurements $\vec{y}$ are redundant to a great extent, due to the sub-optimal combination of uniform distribution of the apertures and uniform 2D-spatial sampling within each aperture. As a consequence, despite (3) may suffice to ensure $\text{rank}(\boldsymbol{A}) = m$ numerically, clustering of multiple eigenvalues around zero will occur, effectively destabilizing the inverse problem. Consequently, rank-awareness becomes key. The latter can be attained leveraging a truncated singular value decomposition of $\boldsymbol{A}$, namely $\boldsymbol{A} = \boldsymbol{U}\boldsymbol{\Sigma}\boldsymbol{V}^*$, where $\boldsymbol{U}$ and $\boldsymbol{V}$ are unitary matrices and the diagonal elements of $\boldsymbol{\Sigma}$, σ_i, are the singular values of $\boldsymbol{A}$. Then, the truncated SVD (t-SVD) solution can be obtained as:

$$\hat{\vec{x}} = \sum_{k=1}^{K} \frac{\langle \vec{u}_k, \vec{y} \rangle}{\sigma_k} \vec{v}_k \iff \hat{\vec{x}} = \boldsymbol{V}_{:,\Omega_{\text{LR}}} \boldsymbol{\Sigma}^{-1}_{\Omega_{\text{LR}}} \boldsymbol{U}^\top_{:,\Omega_{\text{LR}}} \vec{y}, \quad (6)$$

where $\Omega_{\text{LR}} \coloneqq \{1, \ldots, K\}$ with K set to meet some requirement on data explainability. We set the minimum K : $\sum_{k \notin \Omega_{\text{LR}}} \sigma_k^2 / \sum_{k=1}^{K} \sigma_k^2 < 10^{-3}$, i. e., the fewest eigenvalues necessary to retain 99.9% of $\|\boldsymbol{A}\|_2$.

4) Sparsity-aware Estimation: The solutions provided by (5) and (6) ignore relevant prior knowledge on $\vec{x}$, namely, its natural sparsity due to the negligible contributions of objects with poor THz reflectivity, tilted reflective surfaces, or distant scatterers. Acknowledging the sparsity of $\vec{x}$ turns the inverse problem into a linearly-constrained ℓ_0 minimization, which is known to be NP-hard. However, under certain conditions, its convex relaxation, namely, a linearly-constrained ℓ_1 minimization, converges to the same solution [12] and, thus, the optimization reads:

$$\hat{\vec{x}} = \arg\min_{\vec{x}} \|\vec{x}\|_1 \quad \text{subject to} \quad \vec{y} = \boldsymbol{A}\vec{x}, \quad (7)$$

which is known as the *basis pursuit* (BP) problem in CS. In order to account for measurement noise and model mismatch, the equality constraint can further be relaxed into an inequality on the ℓ_2 norm, yielding the basis pursuit denoising (BPDN) problem:

$$\hat{\vec{x}} = \arg\min_{\vec{x}} \|\vec{x}\|_1 \quad \text{subject to} \quad \|\boldsymbol{A}\vec{x} - \vec{y}\|_2 \leq \varepsilon, \quad (8)$$

where ε is set to be coincident with that in (3). We use the SPGL1 library [13] for solving (7) and (8). SPGL1 leverages a method based on root-finding on the Pareto frontier induced by the two-objective optimization in (8) [14].

IV. Experiments and Results

A. Data Acquisition Procedure

In this study, the imaging target domain is a virtual cube created by a precise movement of a THz source controlled by a Universal Robot UR5e. The robot is configured with a 0.5 Kg payload capacity and a 200 ms sleep-time between each movement to ensure precise positioning. To construct a virtual cube of $R_x \times R_y \times R_z = L^3\text{cm}^3$, the robot is programmed to navigate uniformly across a 3D grid. At each grid point, a camera array of $P \times Q$ units records an image of the THz source. To improve the Signal-to-Noise Ratio (SNR), the camera averages $N_{\text{acq}} = 10$ acquisitions per position. These images are then saved with a resolution of $(P \times n_{\text{rows}}) \times (Q \times n_{\text{cols}})$ pixels. Afterwards, every recorded 2D image is transformed into a single vector $\vec{y_i} \in \mathbb{R}^m$. The initial sensing matrix, $\boldsymbol{A_0}$, is then defined as in (2). In our experiment, the parameters are set as follows: The edge of the virtual cube is $L = 8\,\text{cm}$. Adopting a step size of $\Delta = 0.8\,\text{cm}$, the total number of grid points is $n = 11^3$. The distance between the cube's center and the camera array is $d = 24\,\text{cm}$. These experimental parameters are chosen carefully to align

with the emission characteristics of the THz radiation source, ensuring sufficient signal strength at all grid points.

B. Robustness to Measurement Noise

For this analysis on noise robustness, the imaging object comprises eight randomly positioned points within the cube's volume, corresponding to a sparsity level of $s_{\mathrm{GT}} = 8$, as shown by the blue points in Fig. 1. The measurement vector is $\vec{y} = \boldsymbol{A}\vec{x}$.

To examine the algorithm's performance under various noise conditions, we add white Gaussian noise to the measurement vector $\vec{y} = \boldsymbol{A}\vec{x} + \vec{n}$. The image is then reconstructed using the noisy measurement vector. The evaluation of the reconstruction methods is quantified by plotting the Normalized Root Mean Square Error (N-RMSE) versus the SNR in decibels (dB), as illustrated in Fig. 2.

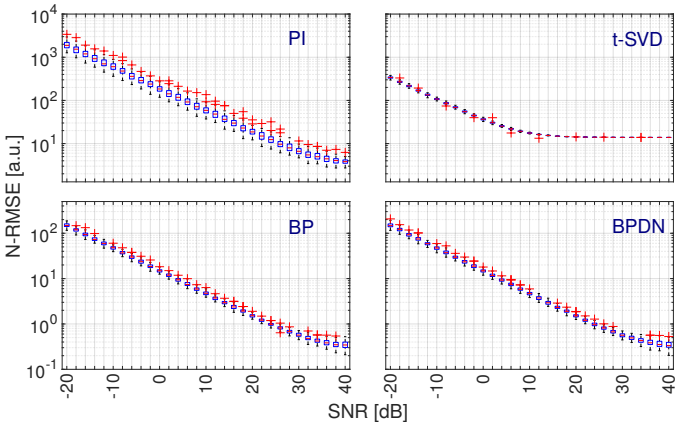

Fig. 2: Analysis of the reconstruction error obtained for the four reconstruction methods under varying noise levels, with sparsity level set at $s_{\mathrm{GT}} = 8$.

The PI method shows improved performance as SNR rises from -20 to 35 dB, highlighting a high sensitivity to noise. At about 35 dB, the error stabilizes, signaling a saturation point where image reconstruction is no longer noise-limited. Conversely, the t-SVD method reduces the impact of noise by discarding minor singular values and vectors, but it saturates earlier, around 10 dB. This early saturation points to limitations from the truncation process, including information loss from disregarded smaller singular values due to the rank selection for the approximation (see top-right plot in Fig.2).

Both Basis Pursuit (BP) and Basis Pursuit Denoising (BPDN) significantly outperform PI and t-SVD methods, showing a substantial reduction in normalized error across the same SNR range, as illustrated in Fig. 2-bottom. This is because they are designed to exploit the inherent sparsity of the target.

Furthermore, PI and t-SVD offer faster computational times of 0.0353 and 0.0441 seconds respectively but struggle with accurate image reconstruction in noisy conditions. Conversely, BP and BPDN deliver better imaging fidelity but require longer times of 1.1148 and 1.1338 seconds. Future research will focus on enhancing PI and t-SVD accuracy through a Coarse-to-Fine approach to leverage their reduced computational demand.

C. Effect of Target Sparsity

The effect of target sparsity on the reconstruction accuracy varies among different algorithms. For both PI and t-SVD methods, the normalized error remains notably constant (N-RMSE $\approx 10^0$) over a sparsity range of $s_{\mathrm{GT}} \in [1, 2^3]$. Beyond the sparsity level $s_{\mathrm{GT}} > 2^3$, the error increases rapidly, demonstrating a threshold effect. This behavior is illustrated in the top plots of Fig. 3.

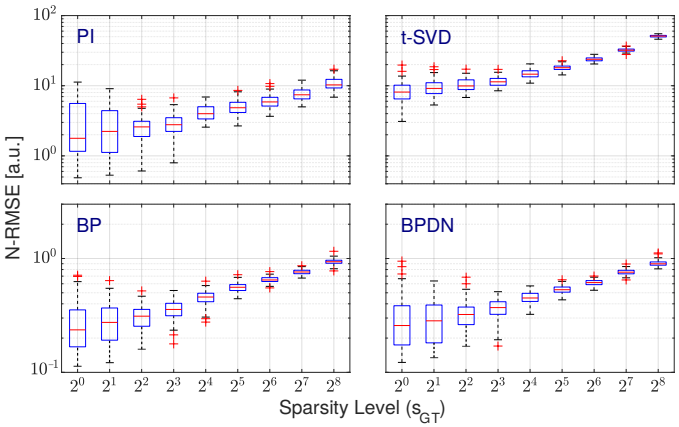

Fig. 3: Impact of the sparsity level s_{GT} on the reconstruction error for the four methods considered, with SNR = 40 dB.

As mentioned previously, the BP and BPDN methods are specifically designed to exploit sparsity. They exhibit the same threshold effect behavior but demonstrate a significantly reduced normalized error (N-RMSE $\approx 10^{-1}$), as demonstrated in the bottom plots of Fig. 3. Throughout these experiments, we systematically increase the sparsity level from $s_{\mathrm{GT}} = 1$ to 2^8, progressively adding more nonzero elements to the ground truth vector while maintaining a constant SNR of 40 dB. This approach tests the algorithm's efficiency in handling higher densities of active elements under consistent noise conditions.

D. Reconstruction of Non-punctual Targets

The evaluations in Sections IV-B and IV-C initially focused on punctual targets to derive general performance indicators. To address the performance on more complex 3D targets with spatial signal clustering, we utilize the MNIST dataset [15]. We assess reconstruction performance using RMSE for 3D targets formed by rotating scaled MNIST images at angles of $\alpha \in \{-45°, 0°, 45°\}$. RMSE statistics are compiled over $N = 10^4$ MNIST images.

The results, including N-RMSE and execution times for the methods, are shown in Fig. 4. Additionally, Fig. 5 features 3D renderings of the reconstructed volumes for one dataset instance featuring the handwritten number "4". Notably, BP and BPDN show similar reconstruction quality, whereas PI and t-SVD struggle with 3D shape recovery due to inadequate regularization.

Target Sparsity	N-RMSE per Percentile [a.u.]			
	0-75%	75-85%	85-95%	95-99%
1	**0.2143**	0.4184	0.4865	**0.5506**
2	0.2400	**0.3820**	**0.4536**	0.5575
4	0.3101	0.4326	0.4775	0.5588
8	0.3412	0.4556	0.5232	0.5648
16	0.4510	0.5474	0.5516	0.5891

TABLE I: Percentile normalized RMSE obtained when using BPDN to reconstruct punctual targets of varying sparsity.

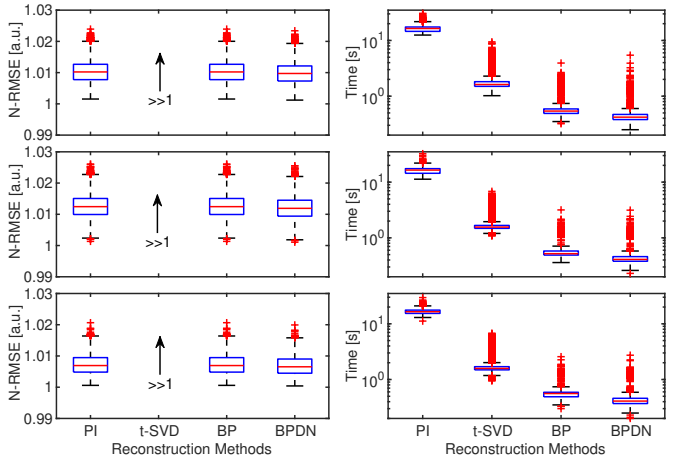

(a) Reconstruction Error (b) Recovery Time

Fig. 4: Normalized RMSE and execution time obtained for three rotations ($-45°, 0°, 45°$, per rows) of 10^4 targets from the MNIST dataset.

V. Conclusions

In this work, we have shown that novel multi-aperture FPAs of THz detectors, combined with tailored algorithmic tools, allow for single-shot 3D THz imaging. The first provides unprecedented measurement diversity, while the second embeds valuable *a priori* knowledge, such as rank-awareness or target sparsity. We have conducted an extensive validation of the performance of reconstruction methods of varying complexity under different conditions, including noise level, target sparsity, and the reconstruction of non-punctual targets. We observed that while the PI and t-SVD methods offer moderate performance in signals characterized by low noise and low sparsity levels, they exhibit limitations in handling signals with high noise or high sparsity levels. In contrast, the BP and BPDN methods demonstrate higher efficiency and robustness, maintaining lower normalized errors compared to the previous two approaches. Moreover, the examination of non-punctual targets using the MNIST dataset highlighted the challenges of reconstructing realistic 3D objects that exhibit spatial clustering. Here, the BP and BPDN models proved again their effectiveness in achieving high-quality reconstructions. Conversely, the PI and t-SVD methods failed due to their lack of an appropriate regularization mechanism. In future work, we plan to extend our investigation to include the challenges presented by dynamic scene reconstruction in 3D THz imaging.

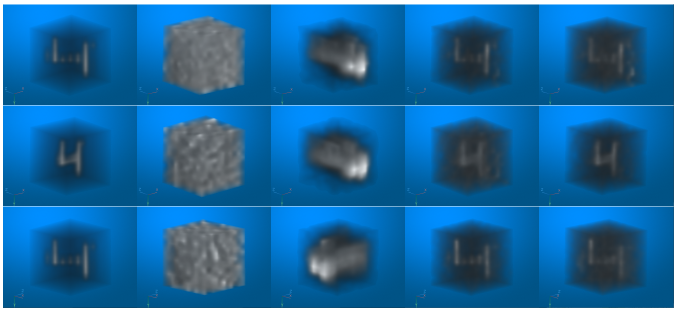

(a) GT (b) PI (c) t-SVD (d) BP (e) BPDN

Fig. 5: Surface rendering of the 3D reconstructions obtained by the four reconstruction methods considered for different rotations ($-45°, 0°, 45°$, per rows) of a sample MNIST image.

References

[1] E. J. Candès, J. Romberg, and T. Tao, "Robust uncertainty principles: exact signal reconstruction from highly incomplete frequency information," *IEEE Transactions on Information Theory*, vol. 52, no. 2, pp. 489–509, Feb. 2006.

[2] E. J. Candès, "Compressive sampling," in *Proceedings oh the International Congress of Mathematicians*, Aug. 2006, pp. 1433–1452.

[3] D. L. Donoho, "Compressed sensing," *IEEE Transactions on Information Theory*, vol. 52, no. 4, pp. 1289–1306, Apr. 2006.

[4] M. Duarte, M. Davenport, D. Takhar, J. Laska, T. Sun, K. Kelly, and R. Baraniuk, "Single-pixel imaging via compressive sampling," *Signal Processing Magazine, IEEE*, vol. 25, pp. 83 – 91, 04 2008.

[5] S. Augustin, P. Jung, S. Frohmann, and H.-W. Hübers, "Terahertz dynamic aperture imaging at standoff distances using a compressed sensing protocol," *IEEE Transactions on Terahertz Science and Technology*, vol. 9, no. 4, pp. 364–372, 2019.

[6] R. I. Stantchev, X. Yu, T. Blu, and E. Pickwell-MacPherson, "Real-time terahertz imaging with a single-pixel detector," *Nature Communications*, vol. 11, no. 1, p. 2535, May 2020. [Online]. Available: https://doi.org/10.1038/s41467-020-16370-x

[7] A. Ndagijimana, M. Heredia Conde, and I. E. Urzainqui, "Performance evaluation of spatial modulation patterns in compressive sensing terahertz imaging," in *2022 IEEE Sensors*, 2022, pp. 1–4.

[8] M. Burger, J. Föcke, L. Nickel, P. Jung, and S. Augustin, "Reconstruction methods in thz single-pixel imaging," in *Compressed Sensing and Its Applications: Third International MATHEON Conference 2017*. Springer, 2019, pp. 263–290.

[9] N. Lyu, J. Zuo, Y. Zhao, and C. Zhang, "Terahertz synthetic aperture imaging with a light field imaging system," *Electronics*, vol. 9, no. 5, p. 830, 2020.

[10] U. R. Pfeiffer and A. Kutaish, "Terahertz light-field imaging with silicon technologies," *IEEE Open Journal of the Solid-State Circuits Society*, vol. 4, pp. 1–11, 2024.

[11] H. Zhang, B. Su, J. He, C. Zhang, Y. Wu, S. Zhang, and C. Zhang, "Light field imaging and application analysis in THz," in *2017 International Conference on Optical Instruments and Technology: IRMMW-THz Technologies and Applications*, C. Zhang, X.-C. Zhang, Z. Huang, and L. Dong, Eds., vol. 10623, International Society for Optics and Photonics. SPIE, 2018, p. 106230O. [Online]. Available: https://doi.org/10.1117/12.2295540

[12] D. L. Donoho, "For most large underdetermined systems of linear equations the minimal ℓ_1-norm solution is also the sparsest solution," *Communications on Pure and Applied Mathematics*, vol. 59, no. 6, pp. 797–829, 2006. [Online]. Available: https://onlinelibrary.wiley.com/doi/abs/10.1002/cpa.20132

[13] E. van den Berg and M. P. Friedlander, "SPGL1: A solver for large-scale sparse reconstruction," December 2019, https://friedlander.io/spgl1.

[14] ——, "Probing the pareto frontier for basis pursuit solutions," *SIAM Journal on Scientific Computing*, vol. 31, no. 2, pp. 890–912, 2008. [Online]. Available: http://link.aip.org/link/?SCE/31/890

[15] L. Deng, "The MNIST database of handwritten digit images for machine learning research," *IEEE Signal Processing Magazine*, vol. 29, no. 6, pp. 141–142, 2012.